Water in Mid Ocean Ridge Basalts: Some Like it Hot, Some Like it Cold

M. Ligi[1], E. Bonatti[1,2], D. Brunelli[1,3], A. Cipriani[2,3], L. Ottolini[4]
1, Institute of Marine Sciences, CNR, Bologna, Italy
2, Lamont-Doherty Earth Observatory, Columbia University, Palisades, New York, U.S.A.
3, Department of Earth Sciences, University of Modena, Modena, Italy
4, Institute of Geosciences and Earth Resources, CNR, Pavia, Italy
marco.ligi@bo.ismar.cnr.it

Abstract

The presence in the Earth's mantle of even small amounts of water and other volatiles has major effects: first, it lowers drastically mantle's viscosity, thereby facilitating convection and plate tectonics; second, it lowers the melting temperature of the rising mantle affecting the formation of the oceanic crust. H_2O concentration in oceanic basalts stays below 0.2 wt% except for basalts sampled near "hot spots" that contain significantly more H_2O than normal MORB, implying that their mantle plume sources are unusually H_2O-rich. Basalts sampled in the Equatorial Atlantic close to the Romanche transform, a thermal minimum in the Ridge system, have a H_2O content that increases as the ridge is cooled approaching the transform offset. These basalts are Na-rich, being generated by low degrees of melting of the mantle, and contain unusually high ratios of light versus heavy rare earth elements implying the presence of garnet in the melting region. H_2O enrichment is due not to an unusually H_2O-rich mantle source, but to a low extent of melting of the upwelling mantle, confined to a deep wet melting region. Numerical models predict that this wet melting process takes place mostly in the mantle zone of stability of garnet. This prediction is verified by the geochemistry of our basalts showing that garnet must indeed have been present in their mantle source. Thus, oceanic basalts are H_2O-rich not only near "hot spots", but also at "cold spots".

1 Introduction

The distribution of water in the interior of our Planet, particularly in the Earth's mantle, has become in the last few years an important objective of the Earth Sciences community. The presence in the mantle of even small amounts of water and other volatiles affects viscosity and partial melting of the mantle that rises below mid ocean ridges, lowering the peridotite solidus and permitting greater melt production at lower mean extents of melting. Melting of the mantle that upwells beneath spreading centers induces significant density and viscosity changes, triggering dynamic upwelling by buoyancy of retained melt and by reduced density of depleted mantle.

The H_2O content of the oceanic upper mantle can be estimated from the H_2O concentration in mid ocean ridge basalt (MORB) glasses correcting for the effects of degassing and magmatic differentiation.

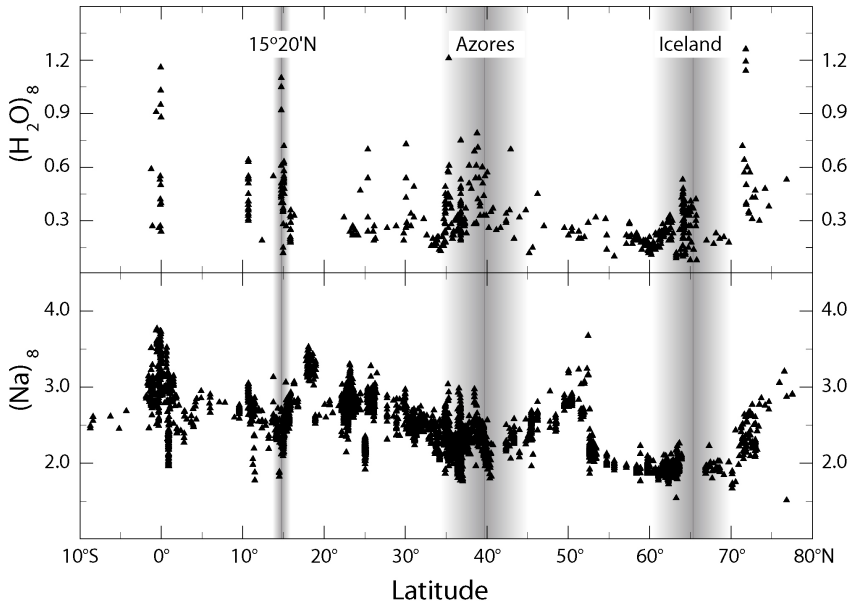

Figure 1: Distribution of Na_8 and $(H_2O)_8$ in MORB glasses along the axis of the Mid-Atlantic Ridge from Iceland to the Equator. Data are from Table 1, our unpublished results and the Petrological Database of the Ocean Floor (PETDB) of Lamont Doherty Earth Observatory.

The H_2O content of normal MORB (N-MORB) is generally below 0.2 wt% [1]. Given that H_2O is about as incompatible as Ce, and assuming $\sim$10% average degree of melting of the mantle upwelling below mid ocean ridges (MOR), the mantle source of N-MORB is assumed to contain 0.01 to 0.02 wt% H_2O [2]. However, basalts from topographically swollen portions of MOR have H_2O concentrations higher than N-MORB (Figure 1). These swollen ridges are generally interpreted as being influenced by hot plumes rising from the transition zone or even deeper in the mantle. Thus, the H_2O content of the mantle source of plume-type oceanic basalts is probably significantly higher than that of the N-MORB source region. For example, the mantle source of the Icelandic [3] and Azores platform [4] crust contain between 620 and 920 ppm, i.e., several times higher than the N-MORB source. Concerning off-ridge hot-spots, a 405 $\pm$ 190 ppm H_2O content has been estimated for the mantle source of Hawaiian basalts [5] supporting the hypothesis that plume-type mantle is H_2O-rich relative to the N-MORB mantle source. High water and volatile contents lower the mantle solidus, so that the mantle melts deeper and to a higher degree during its ascent below MOR.

We report here that the H_2O content of basaltic glasses from the equatorial Mid Atlantic Ridge (MAR) is significantly higher than that of N-MORB [6]. However, these H_2O-rich basalts are associated

not with a "hot" portion of MOR, but with the opposite, i.e. a thermal minimum in the ridge system. We will discuss a model that explains why the H_2O content of oceanic basalt is high not only at "hot spots", but also at "cold spots".

2 Methods

Basaltic glasses were sampled by dredging at several sites along the ∼220 km long MAR segment (eastern Romanche Ridge segment or ERRS) that extends south of the 900 km Romanche transform (Figures 2 and 3). Glasses were selected for freshness and analyzed for Rare Earth element concentrations (REE), H_2O and for major elements. Major elements were determined using a JEOL JXA 8600 microprobe at IGG-CNR, in Florence. The acceleration voltage was 15 kV, the sample current was 10 nA. The counting times were 40 s for Na and Cl and 10 s for all other elements, the spot size was 10 μm. H_2O content was determined at IGG-CNR in Pavia by secondary ion mass spectrometry (SIMS) with a Cameca IMS 4f ion microprobe following a procedure which involves "energy filtered" secondary ions [10] with emission energies in the range 75-125 eV. Under these experimental conditions the H background, measured on a sample of quartz, is typically 0.009 wt% H_2O. The values for H_2O in the Table 1 are the average of 3 measurements. The accuracy of analysis is estimated to be 10% relative. REE were determined with the Pavia ion microprobe. An optimised energy filtering technique [11] was applied to remove complex molecular interferences in the secondary ion mass spectrum. Light REE-rich basalts were analysed applying a deconvolution filter to the secondary-ion REE mass spectrum in order to reduce residual oxide interferences (i.e., BaO on Eu, CeO, NdO on Gd, GdO on Yb, and EuO on Er). Precision of the measure is on the order of 10 % relative, for REE concentrations in the range 0.1-0.7 ppm. Below 0.1 ppm precision is mainly limited by (Poisson) counting statistics and falls to ∼30 % relative. Accuracy is on the same order of precision. The experimental conditions involved a 9.5 nA, 16O- primary ion beam accelerated through -12.5 kV and focused into a spot 10-15 μm in diameter, and energy-filtered (75-125 eV) positive secondary ions detected under an ion image field of 25 μm.

.

3 The Melting Model

We carried out numerical experiments to estimate the extent to which the upper mantle is cooled by a long-offset, low-slip transform, such as the Romanche. The temperature field before the onset of melting has been calculated by the steady-state advection-diffusion equation (1), where k=mantle thermal diffusivity, 8.04 10^{-7} $m^2 \cdot s^{-1}$; v_s=matrix velocity vector; a=adiabatic temperature gradient, 0.0003 °C/m and z=unit vector along z-axis. Mantle temperatures have been computed through a 3D-domain of mantle flow calculations, by the over-relaxation upwind finite difference method described by Morgan and Forsyth [12]), using a variable grid spacing (512x256x101) with the highest grid resolution (1 km) in the proximity of the plate boundaries. Temperature solutions were found assuming constant temperature at the surface (0 °C) and different mantle potential temperatures at 150 km depth in order to evaluate the Equato-

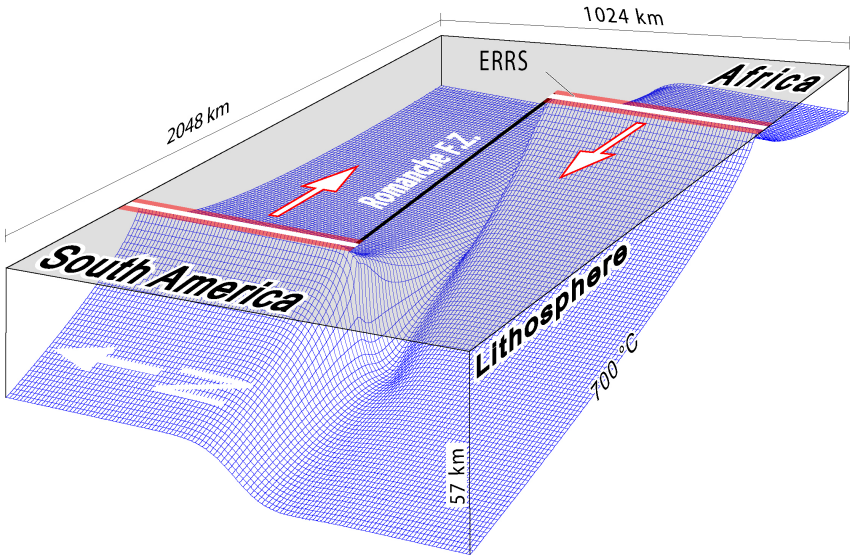

Figure 2: Passive flow model geometry. Base of rigid plates represents the upper boundary layer in our plate thickening passive mantle flow model. It was obtained iteratively solving each time the mantle temperature field, starting from a constant-thickness plate-flow model. The computed thickness of the African plate lithosphere at the ERRS transform intersection is ∼50 km.

rial MAR cold spot effect. Melt parameters of the model (crustal thickness and maximum degree of melting) were inferred from the chemistry of basalts sampled from the centre of the ERRS [8]. A 1330 °C mantle potential temperature has been assumed at a depth of 150 km beneath the ERRS, 50°C colder than "normal" (temperature that produces 6 km of crust, assuming that all melt is extracted).

Mantle flow velocities were estimated in equation (1) assuming steady-state plate thickening passive flow [13, 14]. We modeled the corner flow induced by seafloor spreading in a computational frame 2048x1024 km wide and 150 km deep (2x2 km spaced grid points for each 1 km depth increment) assuming an incompressible, homogeneous, isoviscous mantle beneath a Romanche-like ridge-transform-ridge plate boundary geometry (offset of 900 km) with a spreading rate of 16 mm/yr. We solved for the steady-state three-dimensional passive mantle flow via a Fourier pseudo-spectral technique [15]. The base of rigid plates, assumed to correspond to the depth of 700 °C isotherm, was obtained iteratively solving each time the mantle temperature field, starting from a constant-thickness plate-flow model. A 512 km long ridge segment, longer than the ERRS, was chosen in order to evaluate how far the transform effect extends along axis, avoiding numerical edge effects.

Water in the upper mantle plays an important role in governing melt generation beneath spreading centres [16]. The amount of water present in the oceanic upper man-

Station	D_{FZ} (km)	Depth (m)	Na_8	σ	Fe_8	σ	#	$(Sm/Yb)_n$	σ	#	H_2O (wt%)	$(H2O)_8$	σ	#
1 (S13-11)	41.909	3450	3.43	0.244	9.57	0.197	4	3.52	1.440	4	0.94	0.89		1
2 (S13-12)	43.715	2800	3.31	0.284	8.57	0.621	17	2.20	1.185	14	1.10	1.05	0.109	3
3* (RC2086-18)	43.949	3836	3.46	0.091	6.90	0.116	3	1.62		1				
4 (S16-24)	43.984	3175	3.57	0.037	6.97	0.244	6	1.71	0.046	5	0.64	0.55		1
5 (S16-26)	45.010	2800	3.43	0.127	7.79	0.293	20	1.90	0.199	25				
6 (S13-13)	46.685	3400	3.51	0.297	7.78	0.531	19	1.60	0.056	14	0.68	0.41	0.015	3
7 (S16-27)	47.831	2475	3.32	0.086	8.41	1.256	3	1.42	0.074	3	0.45	0.41		1
8 (S13-14)	49.820	2950	3.27	0.049	8.79	0.164	3	1.79	0.197	3	0.37	0.27		1
9 (S16-25)	50.111	2350	3.50	0.176	7.53	0.670	6	1.73	0.095	6	0.61	0.53		1
10 (S16-28)	53.200	2475	3.14	0.056	6.95	0.207	4	1.80	0.031	5	0.68	0.50		1
11* (RC2086-07)	54.812	4000	3.02	0.020	7.59	0.043	3	2.83		1				
12 (S16-39)	73.138	2550	3.01	0.320	9.18	0.376	4	1.27	0.228	4	0.29	0.25		1
13* (RC2086-16)	74.497	4095	3.09	0.182	9.56	0.557	3	0.75		1				
14 (S16-29)	80.899	3100	2.93	0.272	8.38	0.640	40	1.35	0.115	24	0.27	0.27		1
15 (S16-33)	88.604	2710	3.30		8.33		1	1.70		1				
16 (G96-29)	90.062	5080	3.09	0.095	9.47	0.486	7	1.31	0.039	2	0.25	0.27		1
17* (RC2086-08)	92.973	4220	2.97	0.263	8.90	0.353	2	1.42		1				
19* (RC2086-09)	129.286	4305	2.81	0.025	8.77	0.007	2	1.33		1				

Table 1: Average chemical parameters obtained from basaltic glasses sampled along the ERRS. Samples obtained during cruises S-13, S-16 (RV Akademik N. Strakhov) and G-96 (RV Gelendzik), (this work), and from cruise RC2086 (RV Conrad, Schilling et al. [8]*, trace element compositions from Hannigan et al. [9]).

tle is sufficient to deepen the peridotite solidus [17] and cause partial melting in a region wider and deeper than that expected for an anhydrous mantle [18, 19]. We modeled melt generation, including the effect of water on the peridotite solidus using a modified form of a recent parameterization of experimental data developed by Katz et al. [20], adding a pressure-dependent water bulk distribution coefficient and near-fractional melting regimes. The total amount of melting F, as defined in equation (2), can be expressed as a function of pressure P, temperature T and weight fraction of water dissolved in the melt, where T_s and T_l are the temperatures of the lherzolite solidus and liquidus, respectively. Equation (3) defines the decrease in the solidus temperature caused by a water content X_{H_2O} in the melt, given an initial concentration in the source of $X_{H_2O}{}^{bulk}$ and β, γ and κ are experimentally constrained parameters with values of 1.5, 0.75 and 43 °C $wt\%^{-g}$, respectively.

We assume that peridotite major phases (such as cpx) are never exhausted from the residue, given the low predicted maximum degree of melting (<20%). Release of latent heat of fusion by freezing of melt and hydrotermal cooling have been neglected. Batch and near-fractional melting are assumed and simulated by mapping the melting interval from the batch melting experiments; water is treated as an incompatible component with a bulk distribution coefficient D_{H_2O} that varies with pressure [16]. Thus, the instantaneous dissolved water fraction in the melt is estimated in the case of batch melting and of near-fractional melting model by equations (4a) and (4b), respectively; where equation (5) is the effective bulk partition coefficient with f_0 melt retained. Because ΔT_{H_2O} depends on the melt fraction F, in order to solve the equation (2) we use the Newton-Raphson iterative method, i.e. equation (6).

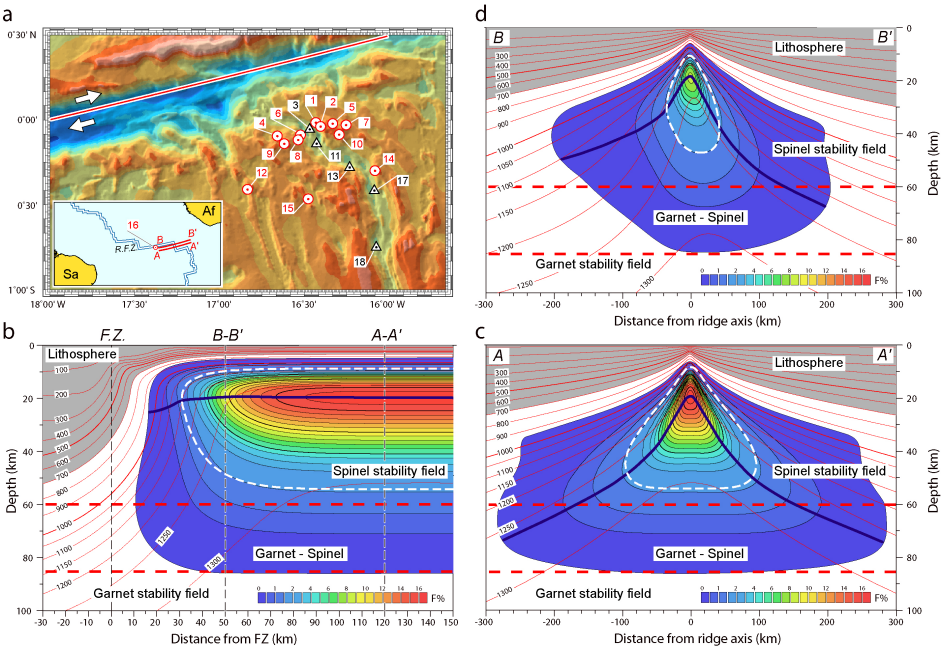

Figure 3: Multibeam topography of the eastern Romanche ridge-transform intersection and predicted melt production beneath the ERRS. a) Shaded relief image based on multibeam data. Depth ranges from 7800 m (dark blue) to 1000 m (light grey). Spreading direction and small circle path (thick red solid line) have been computed using the Africa-South America Eulerian vector of NUVEL-1A model [7]. Sample locations (Table 1) are indicated by red circles (this work) and black triangles. b) Fraction of melt generated along the ERRS axis, including the effect of water on peridotite solidus. White thick dashed line marks the region of dry melting. Solid thick purple line marks the upper boundary of the region of melt production, i.e. where production rate is positive. Red thick dashed lines indicate boundaries between garnet and spinel stability fields. Isotherms are indicated by thin red lines. c) and d) Across axis sections showing fraction of melt generated at the ERRS centre (120 km) and in the proximity (50 km) of the ridge-transform intersection, respectively.

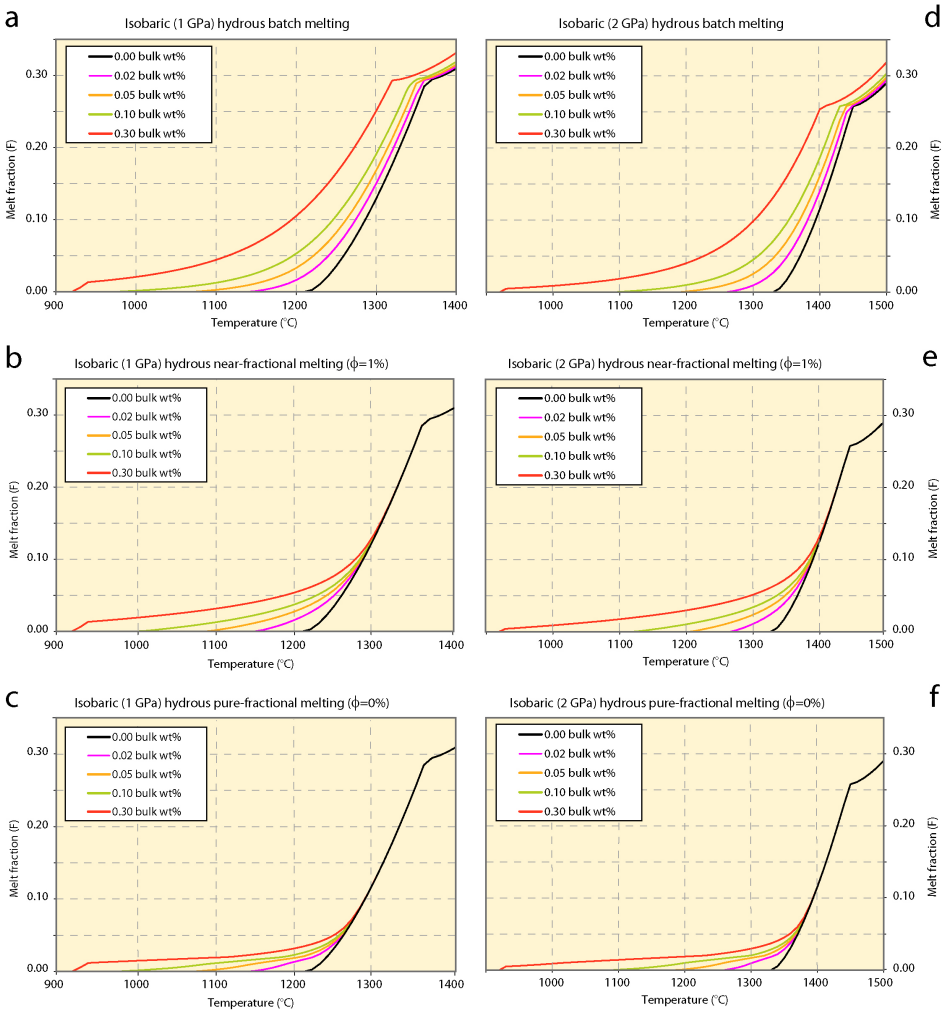

Figure 4: Isobaric melting curves with different bulk water contents and for different melting regimes. We assumed a modal cpx concentration of 17% in the unmelted solid. The discontinuity in melt productivity at high degrees of melting is due to cpx exhaustion. a) Batch melting; b) near-fractional with a residual porosity f=1% and c) pure-fractional at pressures of 1 GPa.; d) Batch melting; e) near-fractional (f=1%) and f) pure-fractional at pressures of 2 GPa. Note, when hydrous melting is included, melting regime affects significantly melt productivity.

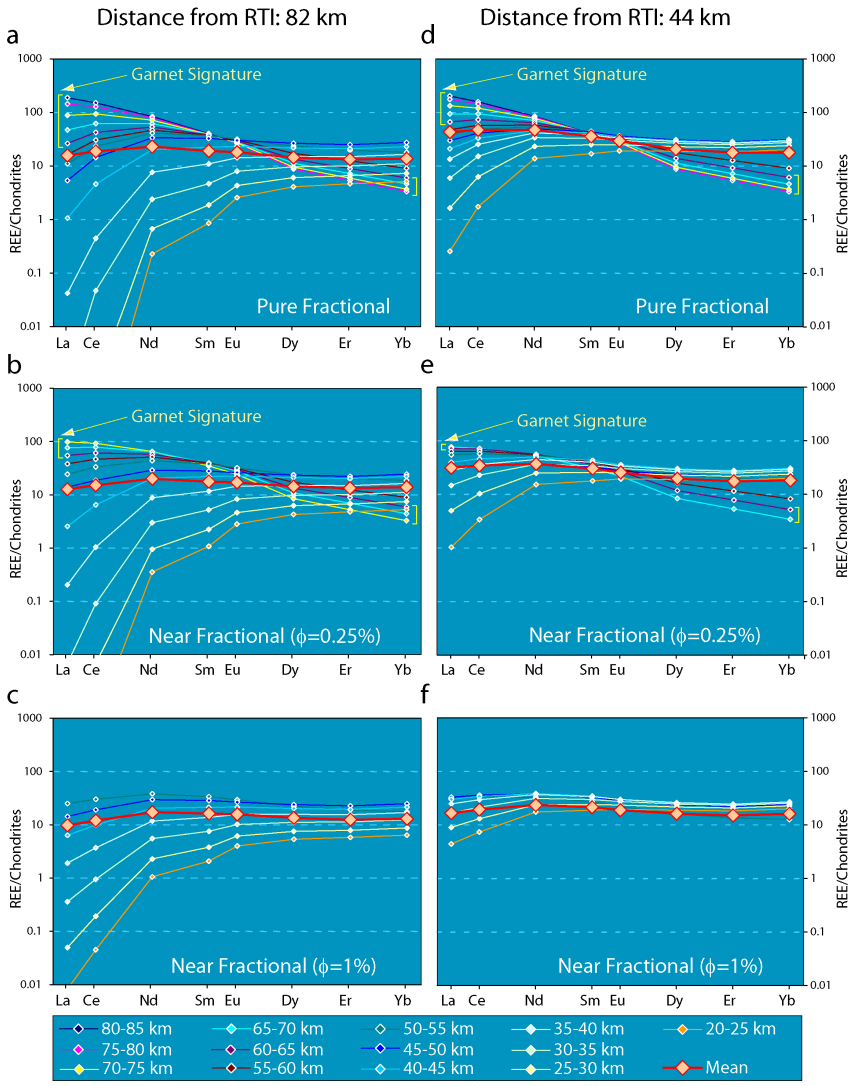

Figure 5: REE patterns, from two different along axis locations, for the near-fractional melting model with different residual porosities. Solid lines connecting small diamonds are partial aggregated melts predicted for vertical increments dz = 5 km. The thick solid red lines connecting big orange diamonds are the mean compositions after complete mixing. Yellow square brackets indicate REE patterns from melt generated in the garnet stability field.

The value of F can be obtained by equation (7), starting with the trial solution F(0) = 0, where *j* indicates the j-th iteration and where the derivative is defined in the case of batch and near-fractional melting models by equations (8a) and (8b), respectively. The convergence of such approximation to the desired solution F can be evaluated by the Banach's contraction mapping theorem: the iteration is terminated when the absolute value of $[(F_{j+1} - F_j)/F_{j+1}]$ is sufficiently small.

Figure 4 shows isobaric melting curves obtained from batch and fractional melting models, at pressures of 1 GPa and 2 GPa, with a constant bulk water distribution coefficient (D_{H_2O}=0.01) and different bulk water contents. Notice that adding water greatly depresses the solidus and produces a prominent "low-F tail" [19]. When water content (0.3 wt% melting curve) exceeds saturation in the melt, which is mostly a function of pressure [20, 21, 22] the melting function sharply increases just above the solidus due to the overabundance of water acting as an additional phase. When major phases, such as cpx, are exhausted from the residue, the productivity decreases discontinuously and then rises again (cpx-out criterium), because melting reactions start to consume principally opx [20]. Note that during batch melting the solid retains incompatible elements, such as water, up to high degrees of melting, thus water affects significantly the maximum extent of melting. In fact, addition of water to a peridotite system increases monotonically the degree of melting at constant temperature and pressure. In contrast, fractional melting determines rapid depletion of water in the residual solid. Melt productivity is low, and only a small percent of the melt fraction is produced before water's complete exhaustion, when melting proceeds above a "dry solidus" with higher production rates [16, 18] reaching the values of dry peridotite [4]. A bulk partition coefficient for water between melt and residue, that decreases during progressive decompression melting because of the drop in pressure and in the modal abundance of pyroxenes [16] yields a sharper wet-to-dry transition than would a constant value of 0.01 of the partition coefficient.

We calculated crustal thickness, mean pressure of melting, mean degree of melting, and mean composition of the aggregate melt, at any locations along axis from the centre toward the tip of the ridge segment, for each of the following melting models: wet and dry, batch, near-fractional and pure-fractional. We assumed as mantle mineral assemblages for garnet, spinel, and plagioclase peridotite those of McKenzie and O'Nions [20] and mineral proportions, in the transition zone between 85 and 60 km, varying linearly from pure garnet peridotite to pure spinel peridotite. REE distribution coefficients and source contents are from Hellebrand et al. [23]. The melt production rate at any place (x,y,z) beneath the ridge is given by equation (9). The total volume of melt production, per unit time per unit length of the ridge , at an along axis location y_0, is given by equation (10) and was computed by integrating equation (9), over the cross-sectional area R in which melting occurs (i.e. over the region where production rate is positive). The crustal thickness H_c is obtained from equation (11), where U_0 is the sea-floor half-spreading rate, rm and rc are mantle and crustal densities, respectively. The mean pressure of melting P was found by integrating the product of the depth and the melt production rate over the melting region R divided by the total melt production rate as in equation (12). The mean de-

gree of melting, in equation (13), was calculated by a similar method, following the definition given by Forsyth [24] and adopting the nomenclature proposed by Plank et al. [25]. The composition of the aggregated melts in equation (14), was estimated by integrating the instantaneous composition of the liquids produced at each degree of melting weighted by the melt production rate, where C_i is the mean concentration of aggregated melt c_i and it is the instantaneous concentration in the liquid for the *i-th* element. Assuming constant solid phase proportions entering in the melt, the bulk distribution coefficient D_i, between liquid and residual solid can be evaluated by equation (15), where X_j is the fraction of the *j-th* mineral and d_{ij} is the partition coefficient for the *i-th* element between the *j-th* phase and liquid. Hence the instantaneous concentration of the*i-th* element, during near-fractional melting, is given by equation (16a), where D_i* is the effective bulk partition coefficient with ϕ_0 melt retained and during batch melting, assuming that melt and solid move together vertically upward, by equation (16b), where F_{max} is the maximum extent of melting at the top of the melting column located at (x, y_0). Figure 5 shows modeled REE patterns from near-instantaneous melts predicted for vertical increments of 5 km at two different along axis locations. The increasing influence of garnet in the aggregate melt, as the ridge-transform intersection is approached, is clearly displayed.

4 Water-rich basalts

The H_2O content of ERRS glasses ranges from 0.25 to 1.10 wt% (Table 1). Their depth of eruption is greater than 2100 m below sea level; thus, they must be undersaturated in H_2O at these depths [21] with little or no H_2O loss during eruption. The absence of vesicles in the glasses supports this conclusion. Their Cl content is $<$0.11 wt% and mostly below the limit of detection (0.04 wt%), suggesting no contamination by sea water. In order to correct for the effects of differentiation, we calculated $(H_2O)_8$, i.e., H_2O normalized to 8 wt% MgO [27, 28], assuming olivine-plagioclase-clinopyroxene fractionation. Fractionation of incompatibles such as H_2O, is better described by power-law equations. We used the equation of Taylor and Martinez [28] to correct H_2O at a common 8 wt% MgO. To limit possible errors introduced by this correction, we used only analyses within the range of 5.5-8.5 wt% MgO. The correction lowers somewhat the H_2O values but does not affect relative trends (Table 1). We used the equation of Plank and Langmuir [26] to correct Na_2O for all the samples, facilitating comparisons of our ERRS data with MORB data. Figure 6 shows FeO versus MgO for all ERRS samples. The data do not show clear fractionation trends, suggesting more than one parental magma or liquid-line-of-descent (LLD). In calculating the corrected FeO values we considered the different quality of the fractionation trends for different sites to account for varying liquid-lines of descent and varying compositions of fractionating FeO. We calculated patterns of LLD for all sites where more than ten analyses are available (Figure 6b), assuming olivine-clinopyroxene-plagioclase fractionation and using the program PETROLOG by Danyushevsky [1], that includes the effects of H_2O on olivine liquidus temperature. From an inspection of the computed LLD patterns, we derived an expression similar to that of Plank and Langmuir [26] for Na_2O, where the frac-

tionation slope increaseas as Fe_8 increases. In evaluating the effectiveness of the estimated local correction, we applied to the data fractionation corrections taken from the literature [27, 28]. Although average values and standard deviation are greatly affected by the fractionation correction we used, the along axis trend is approximately the same. We decide to adopt the expression of Taylor and Martinez [28] due to the small differences with our estimated local correction and to allow comparisons with other water-rich basalts.

$(H_2O)_8$ and Na_8 plotted versus latitude along the MAR axis (Figure 1) reveal variations of basalt water content, with maxima in regions where the MAR is affected by mantle plumes, such as at 62º-70º N (Iceland), 35º-45º N (Azores), and at 15º20' N. Maxima in H_2O content are generally mirrored by minima in Na_8 (Figure 1), consistent with the idea whereby plume-related high degree of melting and water-rich plume mantle source go together [29, 30]. Glasses from the equatorial MAR are an exception to this pattern, in so far as they are H_2O-rich while Na8 is also high. High Na8 basalts are consistent with a low degree of melting in this region [31, 8]. Peridotite mineral composition also suggests that the mantle in the equatorial MAR underwent exceptionally low (<5%) degrees of melting [32], probably due to the combined effect of a regional equatorial Atlantic thermal minimum [31, 29], and of a strong "transform cold-edge effect" [33], that cools the ridge as it approaches old/thick/cold lithosphere across transform offsets.

We carried out numerical experiments to estimate the extent to which the upper mantle is cooled by a long-offset, low-slip transform, such as the Romanche, and how partial melting and H_2O distribution are affected. We assumed a 900 km long transform offset, a half spreading rate of 16 mm/yr and the base of rigid plates determined by the 700 °C isotherm (Figure 2). The ridge segment impacting on the transform was assumed to be 512 km long, longer than the real ERRS, in order to evaluate how far the transform effect extends along axis, avoiding numerical edge effects. Assuming a $\sim$175 ppm H_2O content in the upper mantle [16] the peridotite solidus is lowered causing partial melting in a subridge mantle region wider and deeper than would be if the mantle were dry [18, 19]. We modeled melt generation, including the effect of H_2O on the peridotite solidus, batch and near-fractional melting are assumed and simulated by mapping the melting interval from the batch melting experiments, water is treated as an incompatible component with a bulk distribution coefficient D_{H_2O} that varies with pressure [16].

Our numerical results (Figure 3) show a strong decrease of "crustal production" as the ridge approaches the transform, and no melting at all in a 20-40 km wide strip close to the fracture zone (Figure 3b), in agreement with the observation that the basaltic crust is nearly absent in that strip [32]. A cross-ridge sub-triangular melting region, $\sim$600 km wide at its base, is predicted beneath the centre of the segment, where the maximum extent of melting is 16.5% (Figure 3c). The melting region becomes smaller and asymmetric moving toward the RTI, with the maximum degree of melting decreasing rapidly ($\sim$8% 50 km from the RTI), and the initial depth of melting varying greatly across axis (Figure 3d).

Water addition deepens the onset of melting to 85 km beneath the centre of the segment, too cold for the anhydrous solidus to encounter garnet peridotite. Thus, water

addition allows a significant melt fraction to be generated in the presence of residual garnet (Figure 3c). The initial depth of melting shoals in the proximity of the RTI, where the partially molten region is mostly due to hydrous melting. The numerical model predicts that basalts sampled close to the Romanche fracture zone are generated exclusively in the sub-ridge "wet melting" mantle interval, i.e., between ∼80 and 60 km deep, within the region of stability of garnet. We would thus expect a significant "garnet signature" in the chemical composition of our basalts, since they are undiluted by melts produced in the "dry melting interval", above ∼60 km depth within the spinel stability field.

REE partition coefficients during melting are different across the 80 to 60 km depth boundary between garnet stability below, and spinel stability above: the heavy REE are compatible with garnet but not with spinel. Thus, melting in the garnet stability field produces liquids depleted of HREE relative to LREE, and with (Sm/Yb)n ratios well over one [34, 35, 36, 37] and increasing with the proportion of melt generated in the garnet stability field. The deeper the level where the ascending mantle stops melting, the higher the proportion of melt generated in the presence of garnet [38].

The concentration of highly incompatible elements in the aggregated liquid should be inversely proportional to the mean degree of melting. Therefore, incompatible elements should be increasingly enriched moving along axis towards the RTI. We calculated crustal thickness, mean pressure of melting, mean degree of melting, and mean composition of the aggregate melt, at any location along axis from the centre toward the tip of the ERRS, for each of the following melting models: wet and dry, batch, near-fractional and pure-fractional.

Basalt Na_8, $(Sm/Yb)_n$ and H_2O contents increase along axis toward the RTI, as predicted by the numerical model (Figures 7 and 8). Note that when hydrous melting is included, the selected melting regime (batch, pure or near-fractional) affects melting parameter predictions, due to the pressure release melt parameterization adopted. The observed along-axis average patterns of melting parameter chemical indicators, such as Na_8, Fe_8 and REE concentrations (Figures 7 and 8), suggest that a pure-fractional or near-fractional melting model with a very low residual porosity ($<$0.5 %) fits the data best.

5 Conclusions

We conclude that the H_2O content of the oceanic basaltic crust peaks not only close to "hot spots", but also at "cold spots" along MOR. However, while "hot spot" H_2O maxima are caused by high degrees of melting of their H_2O-rich mantle plume sources, the "cold spots" H_2O enrichment is due to low degrees of melting occurring mostly within the "wet melting" depth interval below the ridge, largely within the garnet stability field, with minor dilution from shallower "dry" melts. Our results are consistent with the ubiquitous presence in the deeper part of the sub ridge melting column of volatiles and enriched components, that are tapped preferentially during incipient "wet" melting, but are normally diluted by more abundant "dry" melts, generated in the shallower part of the melting column. Extrapolating from these results, we expect relatively high H_2O content in basaltic crust generated at other "thermal minima" along the mid Ocean Ridge system, as at the Australian/Antarctic Discordance [39] and at the Gakkel Ridge [40].

6 Acknowledgements

Research sponsored by EUROCORE/EUROMARGINS Programme (Project 01-LEC-EMA21F). Work supported by the Italian Consiglio Nazionale Ricerche, Fondazione Cassa di Risparmio di Modena through CARBRIDGE, and Fondazione Onlus Rita Levi-Montalcini.

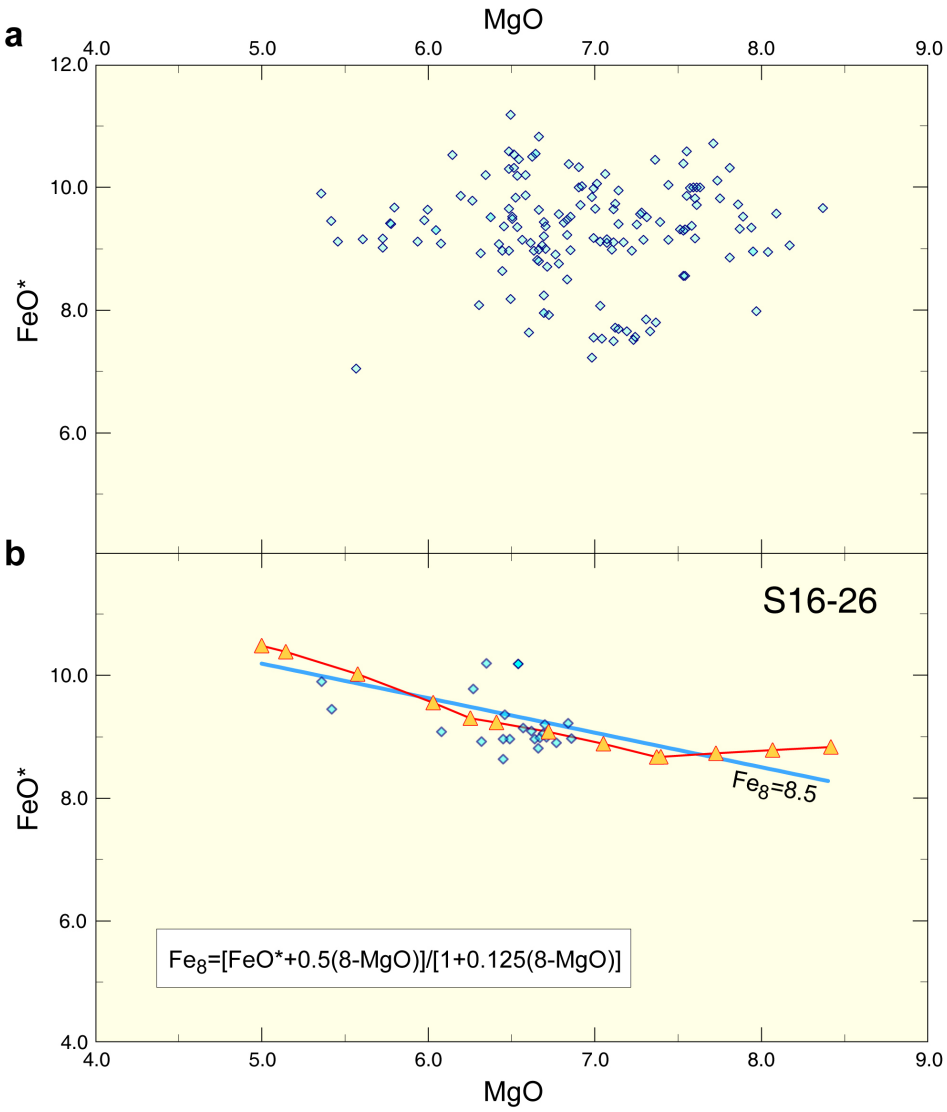

Figure 6: FeO* (FeO total) versus MgO. a) Data from the ERRS basaltic glasess are scattered from linear trends, suggesting more than one parental magma or liquid line of descent (LLD). b) Blue diamonds mark data from site S16-26. Orange triangles and solid red line outline computed LLD for compositions from site S16-26. Solid blue line, slope used to calculate Fe_8.

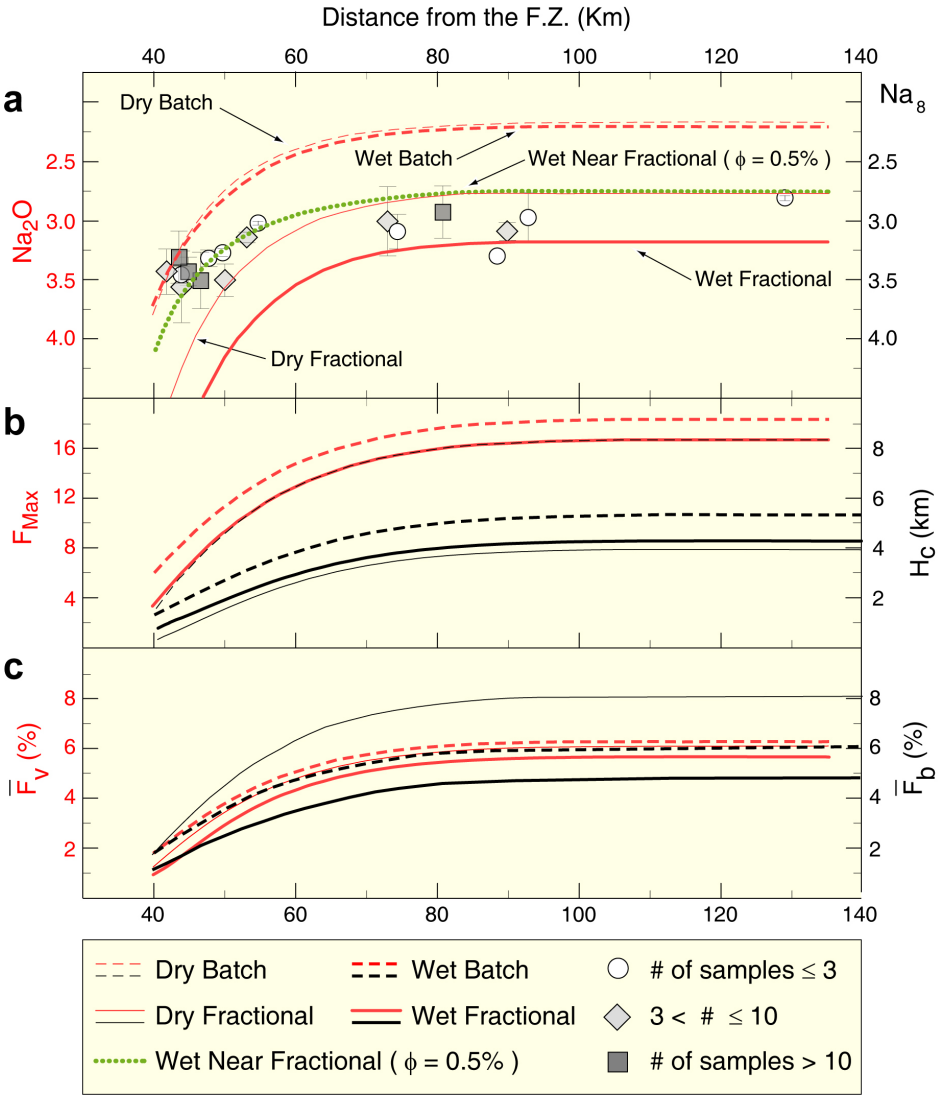

Figure 7: Along axis relationships between different definitions of mean extent of melting (F_V, Forsyth [24] F_B, Plank and Langmuir [26]) and the observables (volume and composition of oceanic crust) for the melting model in Figure 3. a) Average Na_8 of ERRS basaltic glasses and predicted Na_2O concentrations in the aggregated melt assuming source concentration C_0=0.3%, distribution coefficient D=0.03 [26], and different melting regimes. Near fractional melting curve with residual porosity f<0.5% fits the data best. Error bars indicate standard deviation. b) Maximum degree of melting (F_{Max}) and crustal thickness (H_c). c) Mean extent of melting curves: F_B, black and F_V, red lines.

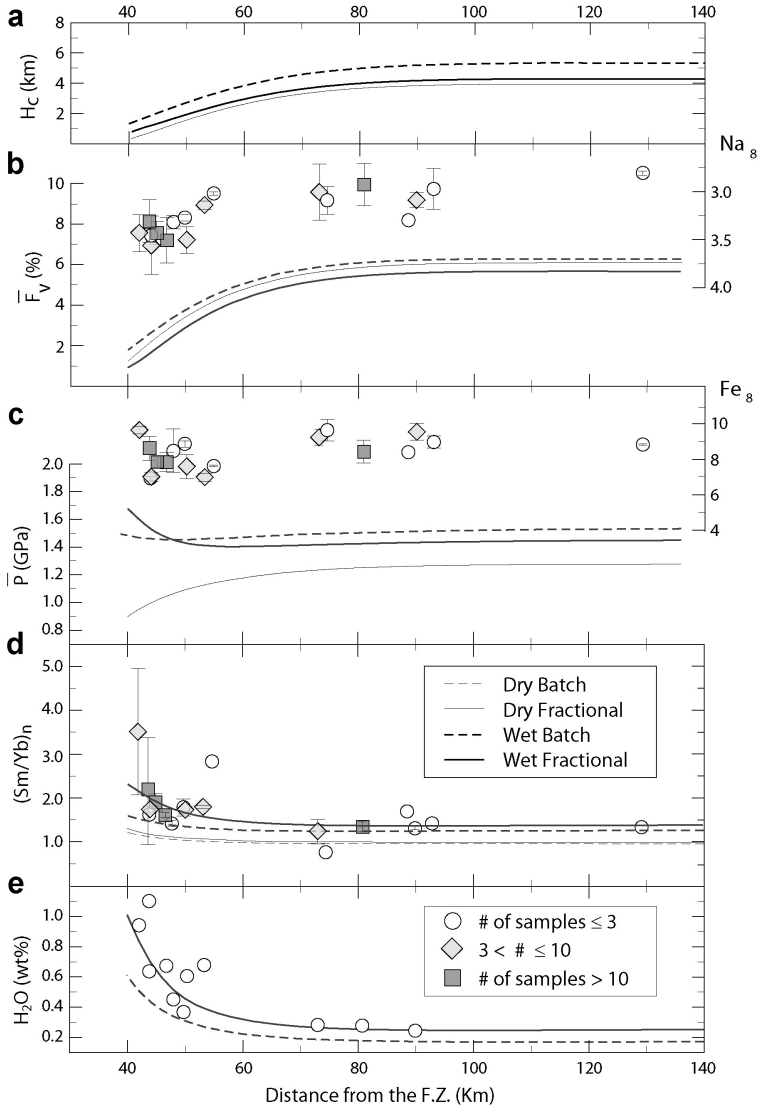

Figure 8: Relationships between melt parameters predicted for mid-ocean ridge melting regimes and values obtained from the basalts sampled along the ERRS axis (Table 1). a) Crustal thickness. b) Average degree of melting and Na_8. c) Mean pressure of melting and Fe_8. Note that left and right vertical axes in b and c are different and independent from each other. d) Chondrite normalized ratio $(Sm/Yb)_n$. e) Models of water content in the aggregated melt and observed H_2O concentrations in basaltic glasses. Error bars indicate standard deviation.

$$\kappa\nabla^2 T = \mathbf{v}_s \cdot \nabla T + \mathbf{v}_s \cdot \alpha\hat{z} \tag{1}$$

$$F(P,T,X_{H_2O}^{bulk}) = \left(\frac{T - T_s + \Delta T_{H_2O}}{T_l - T_s}\right)^{\beta} \tag{2}$$

$$\Delta T_{H_2O} = k\left(X_{H_2O}\right)^{\gamma} \tag{3}$$

$$X_{H_2O} = X_{H_2O}^{bulk} / \left[D_{H_2O} + F(1 - D_{H_2O})\right] \tag{4a}$$

$$X_{H_2O} = X_{H_2O}^{bulk}\left[(1-F)/(1-\phi_0)\right]^{(1/D_{H_2O}^{*}-1)} / D_{H_2O}^{*} \tag{4b}$$

$$D_{H_2O}^{*} = (1-\phi_0)D_{H_2O} + \phi_0 \tag{5}$$

$$f(F) = F - \left[\frac{T - (T_s - \Delta T)}{T_l - T_s}\right]^{\beta} = 0 \tag{6}$$

$$F^{j+1} = F^{j} - \frac{f(F^j)}{f'(F^j)} \tag{7}$$

$$f'(F) = 1 + \frac{\beta\gamma(T-T_s)^{\beta-1}(1-D_{H_2O})\Delta T_{H_2O}}{(T_l - T_s)^{\beta}\left[D_{H_2O} + (1-D_{H_2O})F\right]} \tag{8a}$$

$$f'(F) = 1 + \frac{\beta\gamma(T-T_s)^{\beta-1}(1-D_{H_2O}^{*})\Delta T_{H_2O}}{(T_l - T_s)^{\beta} D_{H_2O}^{*}(1-F)} \tag{8b}$$

$$\dot{m}(x,y,z) = \mathbf{v}_s(x,y,z)\cdot\nabla F(x,y,z) \tag{9}$$

$$\dot{M}(y_0) = \iint_R \dot{m}(x,y_0,z)dxdz \tag{10}$$

$$H_c(y_0) = \frac{\rho_m \dot{M}(y_0)}{\rho_c U_0} \tag{11}$$

$$\overline{P}(y_0) = \frac{\rho_m g}{\dot{M}(y_0)} \iint_R z\dot{m}(x,y_0,z)dxdz + \rho_c g H_c(y_0) \tag{12}$$

$$\overline{F}_V(y_0) = \frac{1}{\dot{M}(y_0)} \iint_R F(x,y_0,z)\dot{m}(x,y_0,z)dxdz \tag{13}$$

$$\overline{C}_i(y_0) = \frac{1}{\dot{M}(y_0)} \iint_R c_i^l(x,y_0,z)\dot{m}(x,y_0,z)dxdz \tag{14}$$

$$D_i = \sum_j X_j d_i^j \tag{15}$$

$$c_i^l(x,y_0,z) = c_i^0\left\{\left[1 - F(x,y_0,z)\right]/\left[1-\phi_0\right]\right\}^{\left[1/D_i^{*}-1\right]} / D_i^{*} \tag{16a}$$

$$c_i^l(x,y_0,z) = c_i^0 / \left\{D_i + F_{\max}(x,y_0)\left[1 - D_i\right]\right\} \tag{16b}$$

Figure 9: Melting model equations

References

[1] L.V. Danyushevsky. The effect of small amounts of H_2O crystallisation of mid-ocean ridge and backarc basin magmas. *J. Volcanol. Geotherm. Res.*, 110:265–280, 2001.

[2] P.J. Michael. The concentration, behavior and storage of H_2O in the suboceanic upper mantle - Implications for mantle metasomatism. *Geochim. Cosmochim. Acta*, 52:555–566, 1988.

[3] A.R.L. Nichols, M.R. Carroll, and A. Hoskuldsson. Is the Iceland hot spot also wet? Evidence from the water contents of undergassed submarine and subglacial pillow basalts. *Earth Planet. Sci. Lett.*, 202:77–87, 2002.

[4] P.D. Asimow, J.E. Dixon, and C.H. Langmuir. A hydrous melting and fractionation model for mid-ocean ridge basalts: Application to the Mid-Atlantic Ridge near the Azores. *Geochem. Geophys. Geosyst.*, 5:Q01E16, 2004.

[5] J.E. Dixon and D.A. Clague. Volatiles in basaltic glasses from Loihi Seamount, Hawaii; evidence for a relatively dry plume component. *J. Petrology*, 42:627–654, 2001.

[6] M. Ligi, E. Bonatti, A. Cipriani, and L. Ottolini. Water-rich basalts at mid-ocean-ridge cold spots. *Nature*, 434:66–69, 2005.

[7] C. DeMets, R.G. Gordon, D.F. Argus, and S. Stein. Effect of recent revisions to the geomagnetic reversal time scale on estimates of current plate motions. *Geophys. Res. Lett.*, 21:2191–2194, 1994.

[8] J.G. Schilling, C. Ruppel, A.N. Davis, B. McCully, et al. Thermal structure of the mantle beneath the Equatorial Mid-Atlantic ridge - Inferences from the spatial variation of dredged basalt glass compositions. *J. Geophys. Res.*, 100:10057–1007, 1995.

[9] R.E. Hannigan, A. Basu, and F. Teichmann. Mantle reservoir geochemistry from statistical analysis of ICP-MS trace element data of equatorial mid-Atlantic MORB glasses. *Chemical Geology*, 175:397–428, 2001.

[10] L. Ottolini, P. Bottazzi, A. Zanetti, and R. Vannucci. Determination of hydrogen in silicates by secondary ion mass spectrometry. *Analyst*, 120:1309–1313, 1995.

[11] P. Bottazzi, L. Ottolini, R. Vannucci, and A. Zanetti. An Accurate Procedure for the Quantification of Rare Earth Elements in Silicates. In SIMS IX Proceedings, edited by A. Benninghoven, Y. Nihei, R. Shimizu and H.W. Werner, John Wiley Sons, Chichester (England). pages 927–930, 1994.

[12] J. Morgan Phipps and D.W. Forsyth. Three-dimensional flow and temperature perturbations due to a transform offset: Effects on oceanic crustal and upper mantle structure. *J. Geophys. Res.*, 93:2955–2966, 1988.

[13] Y. Shen and D.W. Forsyth. The effects of temperature and pressure dependent viscosity on three-dimensional passive flow of the mantle beneath a ridge-transform system. *J. Geophys. Res.*, 97:19717–1972, 1992.

[14] D.K. Blackman and D.W. Forsyth. Mantle Flow and Melt Generation at Mid-Ocean Ridges. *Geophysical Monograph*, 71:311–326, 1992.

[15] M. Ligi, M. Cuffaro, F. Chierici, and A. Calafato. Three-dimensional passive mantle flow beneath mid-ocean ridges: an analytical approach. *Geophys. J. Inter.*, 175(2):783–805, 2008.

[16] G. Hirth and D.L. Kohlstedt. Water in the oceanic upper mantle: Implications for rheology, melt extraction and the evolution of the lithosphere. *Earth Planet. Sci. Lett.*, 144:93–108, 1996.

[17] D.R. Bell and G.R. Rossman. Water in the Earth's mantle: The role of nominally anhydrous minerals. *Science*, 255:1391–1397, 1992.

[18] M.G. Braun, G. Hirth, and E.M. Parmentier. The effect of deep damp melting on mantle flow and melt generation beneath mid-ocean ridges. *Earth Planet. Sci. Lett.*, 176:339–356, 2000.

[19] P.D. Asimow and C.H. Langmuir. The importance of water to oceanic mantle melting regimes. *Nature*, 421:815–820, 2003.

[20] R.F. Katz, M. Spiegelman, and C.H. Langmuir. A new parameterization of hydrous mantle melting. *Geochem. Geophys. Geosyst.*, 4:1073, 2003.

[21] J.E. Dixon and E.M. Stolper. An experimental study of water and carbon dioxide solubilities in mid-ocean ridge basaltic liquids. 2) Applications to degassing. *J. Petrology*, 36:1633–1646, 1995.

[22] B. Mysen and K. Wheleer. Solubility behavior of water in haploandesitic melts at high pressure and temperature. *Am. Mineral.*, 85:1128–1142, 2000.

[23] E. Hellebrand, J.E. Snow, P. Hoppe, and A.W. Hofmann. Garnet-field melting and Late-stage Refertilization in "Residual" Abyssal Peridotites from the Central Indian Ridge. *J. Petrology*, 43:2305–2338, 2002.

[24] D.W. Forsyth. Crustal thickness and the average depth and degree of melting in fractional melting models of passive flow beneath mid-ocean ridges. *J. Geophys. Res.*, 98:16073–1607, 1993.

[25] T. Plank, M. Spiegelman, C.H. Langmuir, and D.W. Forsyth. The meaning of "mean F": claryfying the mean extent of melting at ocean ridges. *J. Geophys. Res.*, 100:15045–1505, 1993.

[26] T. Plank and C.H. Langmuir. Effects of the melting regime on the composition of oceanic crust. *J. Geophys. Res.*, 97:19749–1977, 1992.

[27] E.M. Klein and C.H. Langmuir. Global correlations of ocean ridge basalt chemistry with axial depth and crustal thickness. *J. Geophys. Res.*, 92:8089–8115, 1987.

[28] B. Taylor and F. Martinez. Back-arc basin basalt systematics. *Earth Planet. Sci. Lett.*, 210:481–497, 2003.

[29] J.G. Schilling. Azores mantle blob: The rare-earth evidence. *Earth Planet. Sci. Lett.*, 24:103–105, 1975.

[30] E. Bonatti. Not so hot "Hot Spots" in the oceanic mantle. *Science*, 250:107–111, 1990.

[31] E. Bonatti, M. Seyler, and N. Sushevskaya. A cold suboceanic mantle belt at the Earth's Equator. *Science*, 261:315–320, 1993.

[32] E. Bonatti, D. Brunelli, P. Fabretti, M. Ligi, R.A. Portaro, and M. Seyler. Steady-state creation of crust-free lithosphere at cold spots in mid-ocean ridges. *Geology*, 29:979–982, 2001.

[33] P.J. Fox and D. Gallo. The tectonics of ridge transform intersections. *Tectonophysics*, 104:204–242, 1984.

[34] P. Gast. Trace element fractionations and the origin of tholeitic and alkaline magma types. *Geochim. Cosmochim. Acta*, 32:1057–1086, 1968.

[35] E. Anders and N. Grevesse. Abundances of the elements: Meteoritic and solar. *Geochim. Cosmochim. Acta*, 53:197–214, 1989.

[36] Y. Shen and D.W. Forsyth. Geochemical constraints on initial and final depths of melting beneath mid-ocean ridges. *J. Geophys. Res.*, 100:2211–2237, 1995.

[37] E. Hellebrand, J.E. Snow, H.J.B. Dick, and A.W. Hofmann. Coupled major and trace elements as indicators of the extent of melting in mid-ocean-ridge peridotites. *Nature*, 410:677–681, 2001.

[38] R.M. Ellam. Lithospheric thickness as a control on basalt geochemistry. *Geology*, 20:153–156, 1992.

[39] D.M. Christie, B.P. West, D.G. Pyle, and B.B. Hanan. Chaotic topography, mantle flow and mantle migration in the Australian-Antarctic discordance. *Nature*, 394:637–644, 1998.

[40] P.J. Michael, C.H. Langmuir, H.J.B. Dick, J.E. Snow, et al. Magmatic and amagmatic seafloor generation at the ultraslow-spreading Gakkel ridge, Arctic Ocean. *Nature*, 423:956–961, 2003.